

Design of dual-ligand coordination in metal organic frameworks for breaking the seesaw effect between de- NO_x activity and N_2 selectivity

Kunli Song^a, Jian-Wen Shi^{a,*}, Xinya Zhou^a, Yuwei Gui^a, Jun Li^a, Dandan Ma^a, Yu Chen^a, Chi He^{c,*}, Yufei Jia^a, Bo Qin^a, Liang Liang^a, Yimeng Zhang^a, Yonghong Cheng^a, Shaobin Wang^{b,*}

^a State Key Laboratory of Electrical Insulation and Power Equipment, Center of Nanomaterials for Renewable Energy, School of Electrical Engineering, Xi'an Jiaotong University, Xi'an, Shaanxi 710049, China

^b School of Chemical Engineering, The University of Adelaide, Adelaide, South Australia 5005, Australia

^c Department of Environmental Science and Engineering, State Key Laboratory of Multiphase Flow in Power Engineering, School of Energy and Power Engineering, Xi'an Jiaotong University, Xi'an, Shaanxi 710049, China

ARTICLE INFO

Keywords:

Selective catalytic reduction
Metal-organic frameworks
Dual-ligand coordination
De- NO_x activity
 N_2 selectivity

ABSTRACT

In the selective catalytic reduction (SCR) of NO_x with NH_3 , a catalyst usually exhibits a seesaw effect on de- NO_x activity and N_2 selectivity at low temperatures. Herein, we designed metal-organic frameworks (MOFs) with dual-ligand coordination to regulate the electronic and morphological structure for a breakthrough of the seesaw effect. The developed catalyst attained a noteworthy NO_x conversion exceeding 90% within 60–330 °C with increased N_2 selectivity. The dual-ligand coordination leads to more defects and a more uniform electron distribution for delocalization of electrons, thereby improving de- NO_x activity. Furthermore, the dual-ligand coordination manifests a Si-O-Mn bond for amplifying both de- NO_x activity and thermal stability. Additionally, the dual ligands and Mn produce a hollow sea-urchin-like morphology with more exposed active sites for concentrating reactants and intermediates to improve electron transfer efficiency in N_2 selectivity. This work clarifies the mechanism of dual-ligand regulation for electron-morphology to simultaneously enhance de- NO_x activity and N_2 selectivity.

1. Introduction

NO_x emissions are a paramount environmental concern, with selective catalytic reduction (SCR) standing out as the most efficient method for converting NO_x into N_2 and H_2O . Particularly, low-temperature denitrification (de- NO_x) by NH_3 (LT NH₃-SCR) is advantageous due to its energy efficiency, and low risk of NH_3 oxidation into NO_x . Based on the NO_x emission standards, and safety and environmental friendliness in industrial applications, the catalysts for the LT NH₃-SCR have been widely studied. Currently, the catalysts are mainly transition metal oxides [1,2], mixed-metal oxides [3,4] and zeolites [5,6]. To improve the LT de- NO_x activity of these catalysts, the usual approach is to increase their oxidability to trigger a “Fast SCR” reaction (some NO is oxidized to NO_2 , triggering this reaction: $2\text{NH}_3 + \text{NO} + \text{NO}_2 \rightarrow 2\text{N}_2 + 3\text{H}_2\text{O}$). However, the improvement of oxidability can also easily oxidize NH_3 into N_2O , thereby reducing N_2 selectivity. This brings about a seesaw

effect on de- NO_x activity and N_2 selectivity. Furthermore, these LT de- NO_x catalysts still have poor SO_2 and/or H_2O tolerance, constraining their industrial application.

Recent studies have shown metal-organic frameworks (MOFs) in various catalytic applications, such as photocatalytic hydrogen evolution [7–9], electrocatalytic reduction of carbon dioxide [10,11] and thermocatalytic reduction of nitrogen oxides [12–14]. Substantial explorations have been devoted to the design of MOFs for the application in SCR [15–17], such as loading MOFs with other components or modifying MOFs with metal ions. The loading is usually performed by impregnating or in-situ growth method to distribute another metal or metal oxide on the surface or in the pores of MOFs [18,19]. The modification of metal ions is mainly to replace the coordination metal in MOFs with another one, or to add a metal for a synergy effect with the coordination metal to improve de- NO_x performance [14,20]. Our group has developed a MOF-based catalyst, quasi-Mn-BTC, showing excellent

* Corresponding authors.

E-mail addresses: jianwen.shi@mail.xjtu.edu.cn (J.-W. Shi), chi_he@xjtu.edu.cn (C. He), shaobin.wang@adelaide.edu.au (S. Wang).

LT de- NO_x activity and outstanding SO_2 tolerance, while low N_2 selectivity and poor H_2O tolerance [21]. We further modified quasi-Mn-BTC by adding Fe ions, to improve its resistance to H_2O , but its N_2 selectivity still needs to be enhanced [14]. Usually, the improvement of the oxidation property of the active sites will not only increase the de- NO_x activity, but also cause the oxidation of NH_3 , thus reducing the N_2 selectivity. There is also a lot of research focused on addressing the seesaw effect of activity and N_2 selectivity. Yang et al. [22] used vanadium-modified LiMnO_x to improve de- NO_x activity and N_2 selectivity. Although the ultra-low temperature activity increased from 80% to 100% at 100 °C, the increase in N_2 selectivity was not obvious, and the selectivity was only 70% at 140 °C. Gao et al. [23] studied the positive effect of the introduction of Fe on Mn-Ce de- NO_x activity and N_2 selectivity. Although both improved, the N_2 selectivity dropped to 80% at 240°C. So far, the seesaw effect between de- NO_x activity and N_2 selectivity in LT NH_3 -SCR has not been effectively resolved, using transition metal oxides, MOF-based materials, and other catalysts.

Due to the modifiable pore size, high specific surface area, and ample tunable active sites [24–26], MOF-based catalysts may be most promising in breaking this seesaw effect. Most of previous studies have used a single ligand to design MOFs, which limits their tunability. If dual ligands are introduced, the electronic and morphologic structure of MOFs will be further regulated through dual-ligand competitive coordination [27,28], which is expected to effectively regulate the oxidability of the catalyst so as to break the seesaw effect between de- NO_x activity and N_2 selectivity. However, the dual-ligand coordination design in de- NO_x catalysis remains underexplored.

In the current research, we have constructed a MOF-based catalyst ($x\text{TEOS\&Mn-BTC}$) with dual-ligand coordination for successfully overcoming the seesaw effect between de- NO_x activity and N_2 selectivity. The dual-ligand coordination regulates the electronic structure of a catalyst to enhance the de- NO_x activity, while regulating the morphology to generate a hollow sea urchin-like microsphere structure. Crucially, the dual-ligand regulation limits the oxidation of NH_3 oxidation to N_2O . Additionally, the hydrophobic ethyl group enhances the tolerance of the catalyst to H_2O , and the catalyst has good resistance to SO_2 and H_2O poisoning due to low adsorption energy. Therefore, the obtained $x\text{TEOS\&Mn-BTC}$ catalyst exhibits excellent performance in LT NH_3 -SCR with good SO_2 and H_2O tolerance.

2. Experimental

2.1. Synthesis

The dual-ligand catalyst was synthesized by using two ligands and Mn cation through a hydrothermal method. Typically, different contents (1, 3, 5 and 7 mL) of tetraethyl orthosilicate (TEOS, Aladdin, AR) and 3230 mg of 1,3,5-benzenetricarboxylic acid (BTC, Aladdin, AR) were dissolved into ethanol to get solution A. Then, 1230 mg of manganese acetate tetrahydrate ($\text{C}_4\text{H}_6\text{O}_4\text{Mn}\cdot 4\text{H}_2\text{O}$, Aladdin, AR) was dissolved in ultrapure water to obtain solution B. Subsequently, solution B was slowly poured into solution A, and the mixed solution was transferred into a 200 mL Teflon lined stainless steel reactor, sealed and heated at 110 °C for 18 h. For a typical de- NO_x test, the catalysts were pretreated at 300 °C under a N_2 flow for 2 h, and then heated at 335 °C under air for 6 h.

2.2. Catalytic testing

NO conversion, N_2 selectivity and NH_3 conversion were tested in the reactor at a flow rate of 120 mL/min, containing 500 ppm NO, 500 ppm NH_3 , 5% O_2 , SO_2 (if needed), 6% H_2O (if needed) and N_2 as a balance gas, with 70 mg of catalyst from the temperature of 60–330 °C· H_2O and SO_2 tolerance were also explored at 150 °C.

2.3. Reaction Mechanism

In-situ DRIFT and DFT calculations were utilized to explore the effects of dual-ligand coordination on intermediate products in the reaction process and the regulation of electronic structure.

3. Results and discussion

3.1. Morphological and structural properties

Two ligands were introduced simultaneously in the process of constructing MOF, $x\text{TEOS\&Mn-BTC}$ (x is the concentration of TEOS) (Fig. 1a, Scheme S1, Supporting Information). The coordination center Mn is quickly self-assembled layer-by-layer with the two ligands (TEOS and BTC), and the Si-O-Mn bond was infiltrated into the Mn-O cluster. The two ligands produced a large number of defects (oxygen vacancies, V_0) that can be easy to excite the active sites in the process of competitive coordination, and different coordination states contribute differently to the energy level orbitals, thereby regulating the electronic structure of $x\text{TEOS\&Mn-BTC}$. While enhancing the structural stability of $x\text{TEOS\&Mn-BTC}$, a high-surface area, hierarchically porous structure was also constructed. At the same time, the ethyl groups on the TEOS ligand can also functionalize the $x\text{TEOS\&Mn-BTC}$. Since the hydrolysis of TEOS is related to the ratio of TEOS to H_2O , the degree of hydrolysis and competitive coordination can be adjusted by the content of TEOS [29–32]. In the synthesis process, 1, 3, 5, and 7 mL of TEOS were added, and the resulting catalysts were named as 1TEOS&Mn-BTC, 3TEOS&Mn-BTC, 5TEOS&Mn-BTC and 7TEOS&Mn-BTC, respectively. The detailed synthesis and activation process of catalysts can be found in the Supporting Information (Section 1).

The thermal gravimetric analysis (TGA, Fig. S1), powder X-ray diffraction (PXRD, Fig. S2) and Raman spectra (Fig. S3) affirmed the successful construction of $x\text{TEOS\&Mn-BTC}$. TGA results indicated that the decrease in the quality of the catalysts before 380 °C is mainly attributed to the removal of impurities, water and some organic ligands. The mass decreased sharply after 380 °C, indicating that the structure of the catalysts has collapsed. The catalyst has sufficient thermal stability up to 380 °C. PXRD results indicated that Mn in the catalyst mainly exists in the form of Mn_2O_3 . Furthermore, the Raman test also confirmed the substantial generation of V_0 (660 cm^{-1}) by the catalysts, attributed to the dual-ligand competitive coordination, thereby facilitating the catalytic reaction [33]. By partially removing the organic ligands, a transition-state structure between MOF and metal oxide was established, augmenting the thermal stability of $x\text{TEOS\&Mn-BTC}$ and preserving the flexible regulation of the pore structure [34,35]. The scanning electron microscopy (SEM, Fig. S4) indicated $x\text{TEOS\&Mn-BTC}$ as hollow sea-urchin-like microspheres formed by layer-by-layer self-assembly of crystalline block copolymers in dual-ligand coordination [36–38], which can promote the generation of hierarchical porous structures. This assembly promotes the generation of hierarchical porous structures, enhancing the diffusion of adsorbed species and V_0 production [39,40], but also induce special void confinement effects. Such a structure will enhance the enrichment of reactants, expose more active sites, improve the efficiency of electron transfer, and prevent the shedding of intermediates [41–43].

The transmission electron microscopy (TEM), high-angle annular dark-field scanning transmission electron microscopy (HAADF-STEM) and energy dispersive X-ray spectroscopy (EDX) mapping revealed the overall morphology of $x\text{TEOS\&Mn-BTC}$ (Fig. 1b-o, Figs. S5–7), confirming their hollow sea-urchin-like structure with an interior cavity. To investigate the influence of dual-ligand coordination on the specific surface area and pore structure of MOF, we explored N_2 adsorption-desorption isotherms (Fig. S8a-b, Table S1). For all $x\text{TEOS\&Mn-BTC}$ samples (Fig. S8a), the distinct hysteresis loop between adsorption and desorption branches suggests the existence of mesopores, which is also consistent with the pore size distribution (Fig. S8b, Table S1) [44–46].

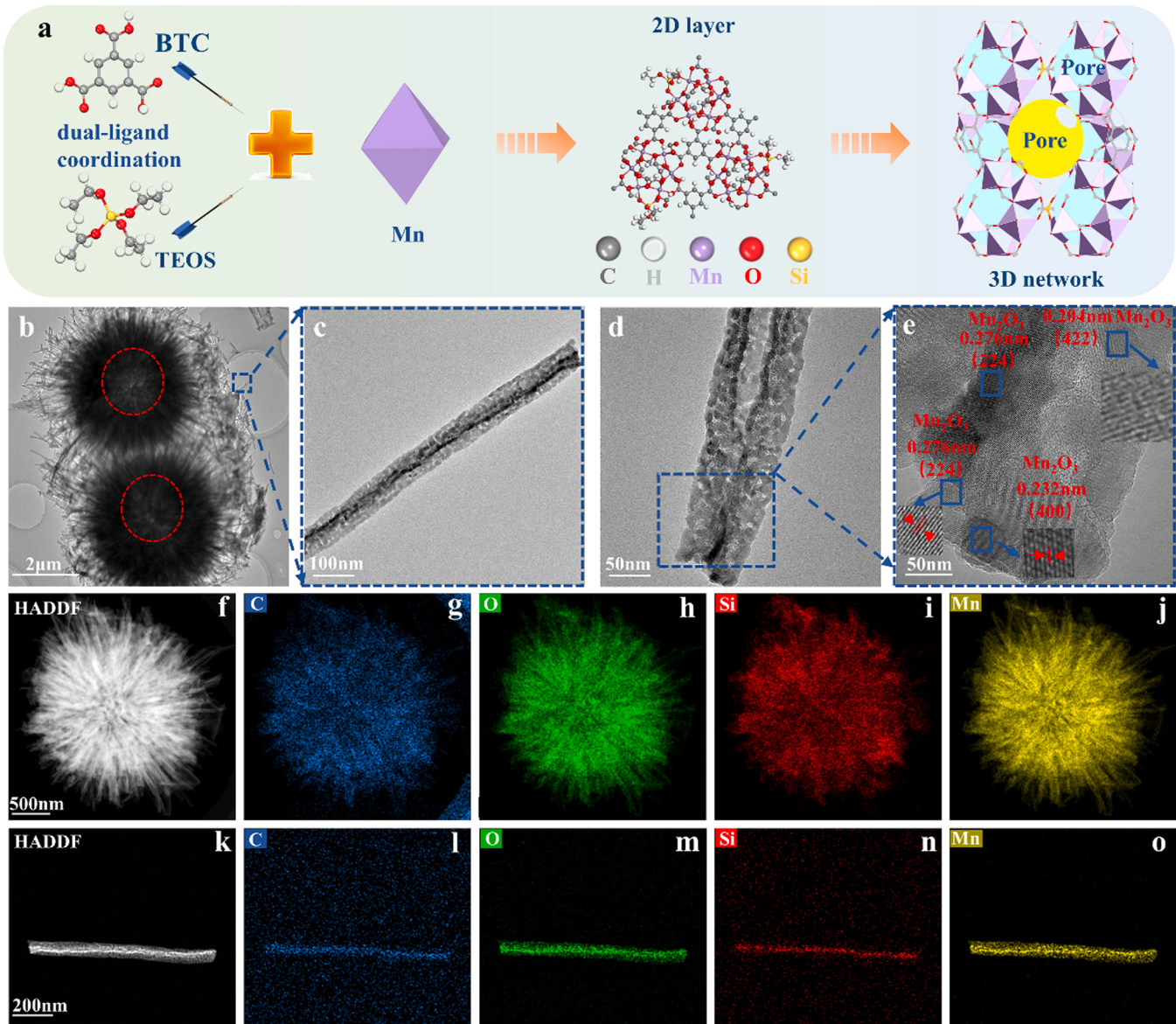


Fig. 1. The dual-ligand coordination illustration of xTEOS&Mn-BTC (a); TEM images of 3TEOS&Mn-BTC (b-e); HAADF-STEM image of 3TEOS&Mn-BTC (f and k) and the corresponding EDX elemental mappings (g-j and l-o) of 3TEOS&Mn-BTC.

Besides, mesopores can also enhance the transport of reactants to catalytic active centers and reduce mass transfer during catalysis [47,48]. Among these catalysts, 3TEOS&Mn-BTC had the largest pore volume, with pore sizes mainly concentrated in the ranges of 1.4–2.0, 3.8–18.5, 18.6–24.4 and 24.4–30.0 nm. By analyzing the particle size distribution of the catalysts (Fig. S8c), it is found that the particle size distributions of 1TEOS&Mn-BTC and 3TEOS&Mn-BTC are more uniform. With the increase of Si element, the polymerization reaction is accelerated, resulting in the increase in particle size and uneven growth of MOF.

Fig. 2a-e show the spectra of X-ray photoelectron spectroscopy (XPS), and the proportions of each element are summarized in Table S2. For C element (Fig. 2a), there was an obvious C-H bond at 284.8 eV [49] derived from the organic ligand of the catalyst and the ethyl group, which is consistent with the peak of Si-CH₃CH₂ in FTIR (Fig. 2f) [50,51]. Among all samples, the C content in 3TEOS&Mn-BTC was the least, because more capping ligands of 3TEOS&Mn-BTC were removed during the calcination process, resulting in more pores and active sites exposed. The phenomenon is consistent with the TGA of 3TEOS&Mn-BTC at the greatest mass loss. The reduced C content is beneficial to enhancing the

catalyst stability and decreasing the catalyst oxidation during the redox reactions.

For Si element (Fig. 2b), no obvious peak was detected due to the low Si content in 1TEOS&Mn-BTC, but obvious Si-O bond and Si-C bond peaks were detected at 100.66 and 102.88 eV in other samples [52,53], which are consistent with the peaks of Si-O-Mn and Si-CH₃CH₂ in FTIR (Fig. 2f). Among these samples, the Si content in 3TEOS&Mn-BTC was the largest, implying the different TEOS contents will lead to different coordination of the two ligands. An increase of TEOS led to hydrolysis reaction, producing SiO₂. It is worth noting that Si-O-Mn bonds are generated in the dual-ligand structure, constructing a coordination with electron-metal-carrier interaction. This structure can significantly adjust the electronic structure of the three-dimensional state of Mn, promote the surface activation of active sites, and also enhance the thermal stability of the catalyst [54,55].

For O element (Fig. 2c), there was an obvious peak at 529.0 eV to be assigned to the lattice oxygen (O_{α}) of Mn_2O_3 [56], which is consistent with the results of PXRD and TEM. The peak assigned to the adsorbed oxygen ($O_{\beta}\text{-O}^2-$) appeared at 530.0 eV, which is conducive to promoting

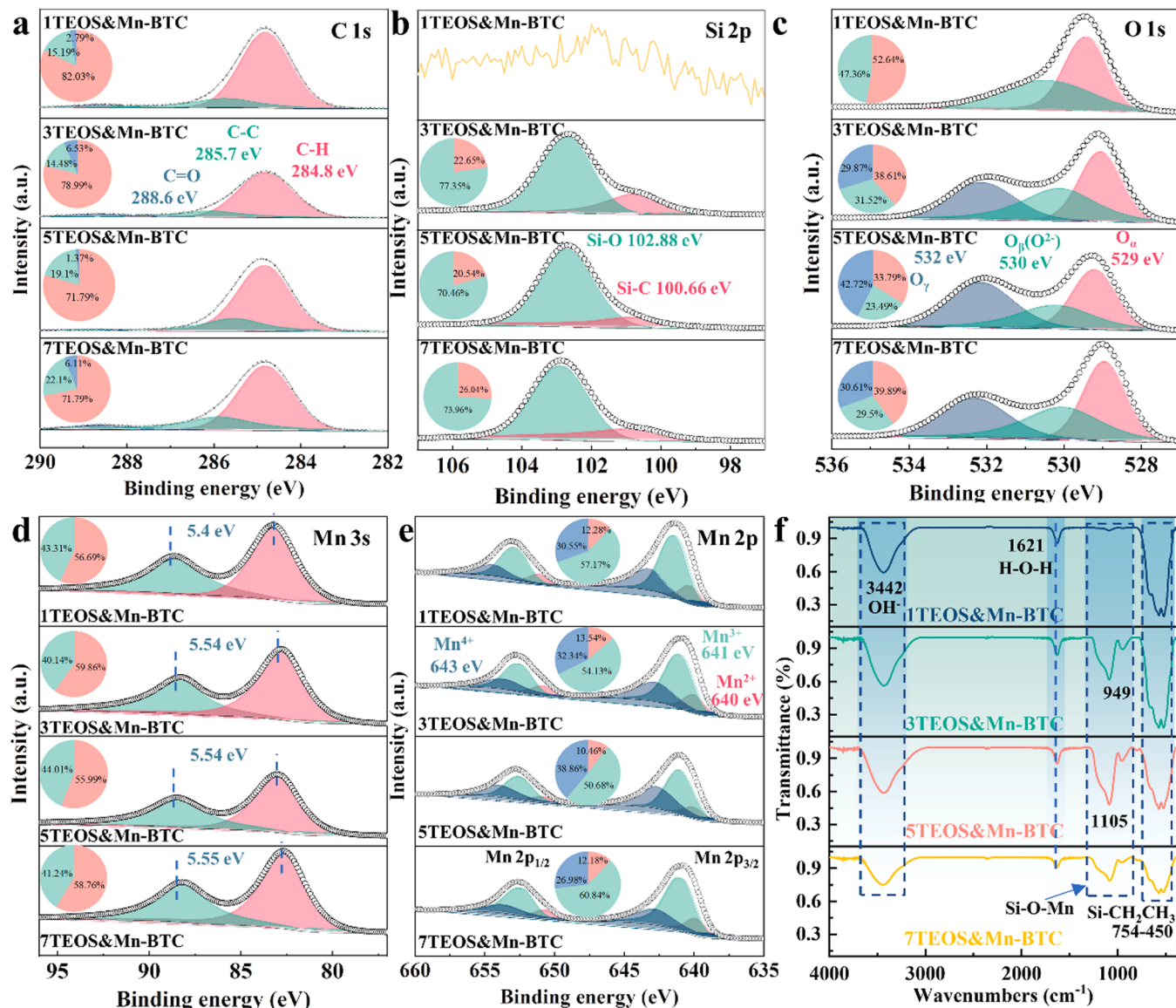


Fig. 2. Physicochemical characterizations of catalysts: XPS spectra of x TEOS&Mn-BTC in the C 1 s region (a), Si 2p region (b), O 1 s region (c), Mn 3 s region (d), Mn 2p region (e) and FTIR spectra of x TEOS&Mn-BTC (f).

electron transport and enhancing catalytic activity [57]. The peak (532.0 eV) of surface-active oxygen (O_a) was also found in most samples except 1TEOS&Mn-BTC. The $O_b(O^{2-})$ and O_c , especially $O_b(O^{2-})$, are crucial to improving the LT de- NO_x performance of the catalysts.

For Mn 3 s (Fig. 2d), there were two split peaks, and the Mn oxidation state can be judged by the degree of Mn 3 s splitting peak, whose value at 5.5 is referred mainly to a mixture of Mn^{3+} and Mn^{4+} [58,59]. Mn 2p spectra (Fig. 2e) suggested the presence of Mn^{2+} , Mn^{3+} and Mn^{4+} [60]. The Mn element gradually decreased with the increased Si content, implying the Si hydrolysis reaction inhibits the coordination between Mn and the dual ligands, and 3 mL of TEOS is the most beneficial for dual-ligand coordination process.

In general, the catalysts are composed of six coordinated Mn element and six oxygens to form a manganese-oxygen octahedron, and then connected through C-C, C-H, C-O, C-Si and Si-O bonds to form a porous framework structure. The C-C, C-H, and C-O bonds are derived from BTC ligands, and C-Si and Si-O are formed from the competition coordination of BTC and TEOS. During the process of competition between the BTC and TEOS for coordination, Si-O-Mn bonds are also formed. The FTIR also proved that Mn was successfully coordinated with the two ligands

to generate x TEOS&Mn-BTC. Moreover, the variance in electronegativity between Si and Mn facilitates the transfer of valence electrons from Mn to Si through O, leaving Mn in an electron-deficient state and resulting in the generation of Lewis (L) acid, which is beneficial for catalytic de- NO_x . Among these catalysts, 3TEOS&Mn-BTC has the most active oxygen species and the greatest stability. It is worth noting that the design of the dual-ligand structure creates an ethyl hydrophobic functional group, which may improve the H_2O tolerance of the catalyst.

3.2. Catalytic performance in SCR

The de- NO_x activity of x TEOS&Mn-BTC was evaluated by NO conversion at a gas hourly space velocity (GHSV) of $36,000\text{ h}^{-1}$. 3TEOS&Mn-BTC had the best de- NO_x performance, with a NO conversion of over 90% in the temperature range of $60\text{--}330\text{ }^\circ\text{C}$ and a NO conversion of 100% at $90\text{--}270\text{ }^\circ\text{C}$ (Fig. 3a). For higher GHSV conditions ($108,000\text{ h}^{-1}$), 3TEOS&Mn-BTC still maintained a NO conversion of more than 80% at $150\text{--}330\text{ }^\circ\text{C}$ (Fig. S9a). The excellent LT de- NO_x activity of 3TEOS&Mn-BTC is attributed to its best coordination between dual ligands and Mn. As discussed from the above characterizations, the

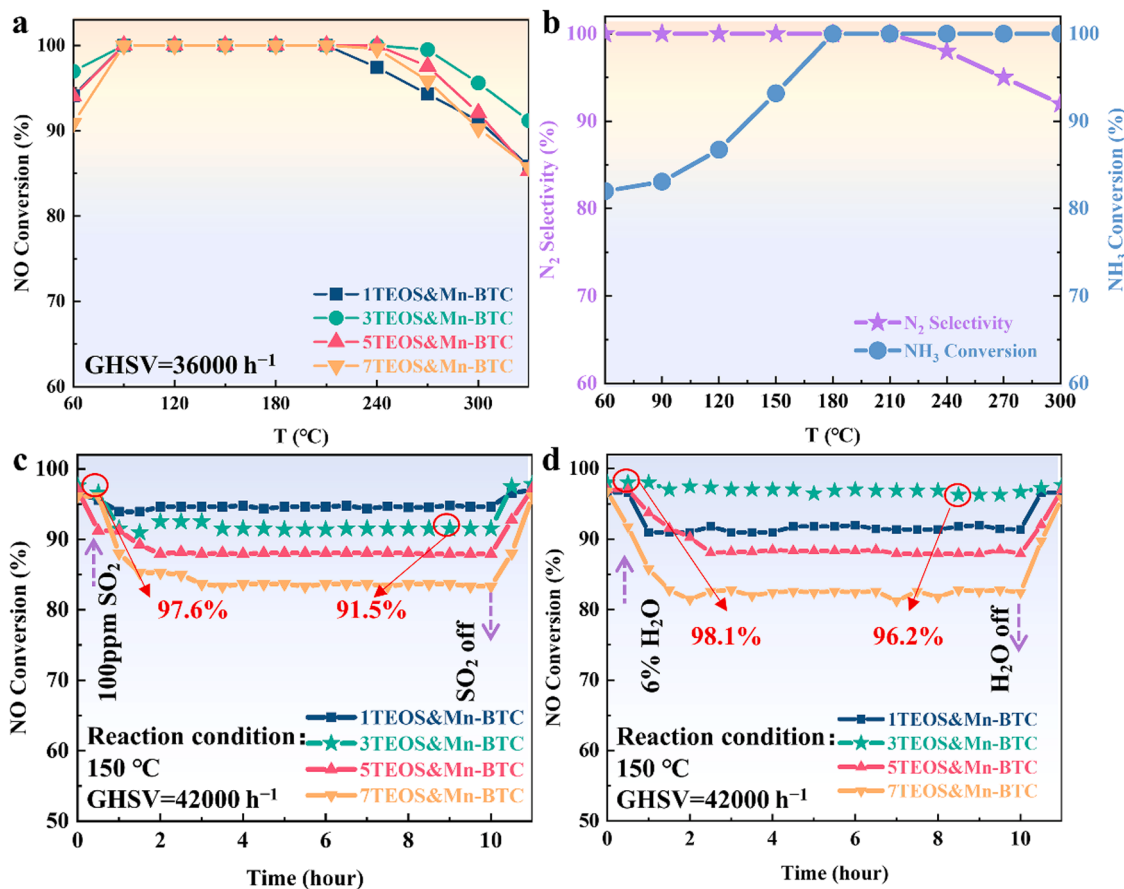


Fig. 3. NH₃-SCR activity: De-NO_x performance of xTEOS&Mn-BTC (a); N₂ selectivity and NH₃ conversion of 3TEOS&Mn-BTC (b); The tolerance of 3TEOS&Mn-BTC to 100 ppm SO₂ (c) and 6% H₂O (d).

dual-ligand coordination will make more defects, formation of the coordination structure of electron-metal-carrier interaction and regulated electronic structure during the dual-ligand coordination, as well as the generation of hollow sea-urchin-like microspheres. 3TEOS&Mn-BTC has the largest specific pore volume, a suitable hierarchical porous structure, and a large number of surface-active oxygen and V_o, which will enrich a large number of reactants on the surface, increase electron transport and avoid the shedding of transition state reactants. In order to further analyze the reaction rate and the apparent activation energy of the catalyst, the de-NO_x activity of 3TEOS&Mn-BTC was tested at the GHSV of 280,000 h⁻¹ (Fig. S9a) to avoid the influence of internal and external diffusion. The reaction rate (Fig. S9b) was calculated using formula (1), and the reaction rates of the 3TEOS&Mn-BTC at 60, 90, 120, 150 and 180 °C were 1.45, 1.66, 2.74, 3.58 and 4.13 mol NO m⁻²s⁻¹ × 10⁻⁷ respectively. According to the Arrhenius equation ($k=A\exp(Ea/RT)$), the apparent activation energy (Ea) can be calculated from the slope of a linear graph with 1000/T as the abscissa and ln(r) as the ordinate (Fig. S9c), and the result was 9.98 kJ/mol.

$$r = \frac{F \times \alpha}{S_{Mn-surf}} \quad (1)$$

Where r is the reaction rate, $S_{Mn-surf}$ is the surface area of the Mn on the surface of the catalysts, α is the conversion rate of NO at the corresponding temperature, F is the flow rate of NO/mol s⁻¹.

N₂ selectivity and NH₃ conversion are important indicators for evaluating de-NO_x performance of catalysts. Compared with our previous study (quasi-Mn-BTC without TEOS) [21], 3TEOS&Mn-BTC exhibited increased N₂ selectivity and good NH₃ conversion (Fig. 3b), indicating that the dual-ligand coordination produced the structure for high reaction efficiency, but not the active site for NH₃ oxidation to N₂O

to balance the activity and selectivity.

The tolerance of xTEOS&Mn-BTC to H₂O and SO₂ was tested at 150 °C and a GHSV of 42,000 h⁻¹. With 100 ppm SO₂, NO conversion of the four samples decreased by 2%-3%, 5-6%, 9-10%, and 12-13%, respectively (Fig. 3c). After SO₂ removal, NO conversion quickly recovered, indicating that the effect of SO₂ is reversible and will not damage the active site of the catalysts. After introducing 6% H₂O (Fig. 3d), NO conversion of the four samples decreased by 5-6%, 1-2%, 8-9% and 13-14%, respectively, due to the competitive adsorption of NO, NH₃ and H₂O. The decrease in NO conversion was completely restored after shutting down H₂O, thus the effect of H₂O on catalytic performance is also reversible. The dual ligands functionalize the MOF with an ethyl group (a hydrophobic functional group), making 3TEOS&Mn-BTC have the best H₂O tolerance. However, 5TEOS&Mn-BTC and 7TEOS&Mn-BTC have poor H₂O tolerance because the different pore structure induced the adsorption of more H₂O. What is more, excessive TEOS leads to hydrolysis, reducing the degree of dual-ligand coordination, ethyl groups and H₂O tolerance. The co-tolerance of H₂O and SO₂ of the catalysts were further explored (Fig. S9d). The reduction in NO conversion caused by H₂O and SO₂ was still reversible, and 3TEOS&Mn-BTC presented the best co-tolerance performance. Compared with similar de-NO_x catalysts reported in the literature, the design of dual-ligand coordination has produced catalysts with excellent de-NO_x activity (Table S3).

The NO oxidation activity of 3TEOS&Mn-BTC was tested at the GHSV of 42,000 h⁻¹ with a flow of 500 ppm NO and 5% O₂ (Fig. S10). It can be found that the NO will be oxidized to generate NO₂ above 150 °C, and the generation of NO₂ will lead to the “Fast SCR” reaction and increase the reaction rate. Although the oxidation of NO to NO₂ was enhanced and more NO₂ was generated above 240 °C, the increase of the

oxidation will also cause the oxidation of NH_3 , which is also one of the reasons why the N_2 selectivity of the catalyst decreased after 240 °C.

3.3. The role of active sites in catalysts

Temperature-programmed reduction experiments with H_2 ($\text{H}_2\text{-TPR}$) were used (Fig. 4a and d) to explore the redox properties. The reduction peaks at 306–341 °C are attributed to the reduction of MnO_2 to Mn_2O_3 , and the peaks at 425–428 °C are attributed to the reduction of Mn_2O_3 to MnO [61,62]. Among the four $x\text{TEOS\&Mn-BTC}$ samples, 1TEOS&Mn-BTC had the most redox sites, and the redox properties of 3TEOS&Mn-BTC were similar to those of 1TEOS&Mn-BTC, implying the more dual-ligand coordination did not enhance the redox of the catalysts, which is also one of the reasons for the high N_2 selectivity of 3TEOS&Mn-BTC. However, when the TEOS content increased to 5 and 7 mL, the redox sites were greatly reduced due to TEOS hydrolysis to SiO_2 , which will cause decreased de- NO_x performance of 5TEOS&Mn-BTC and 7TEOS&Mn-BTC.

Temperature-programmed desorption tests with NH_3 ($\text{NH}_3\text{-TPD}$) and NO (NO-TPD) were also performed to investigate active sites. For $\text{NH}_3\text{-TPD}$ (Fig. 4b and e), there was a main peak between 220 and 380 °C, which was first shifted towards the LT region, and then gradually towards the high-temperature region with the increased TEOS content. The results imply that dual-ligand coordination can indeed generate more NH_3 adsorption sites. For 5TEOS&Mn-BTC and 7TEOS&Mn-BTC, the decrease in adsorption sites can be ascribed to the hydrolysis caused by excessive TEOS, which prevents Mn from fully coordinating with the two ligands. Moreover, SiO_2 produced by hydrolysis will also deposit on the surface of the catalyst, covering the active site. Therefore,

3TEOS&Mn-BTC has the most amounts of NH_3 adsorption sites for its best performance. The higher the temperature corresponding to the peak, the stronger the acidity. Generally, those below 200 °C represent weak acid sites, those above 400 °C denote strong acid sites, and those between 200 and 400 °C are classified medium acid sites. Therefore, the acid sites of the catalysts are all medium acid sites. The test results indicated that the design of the dual-ligand structure will weaken the strength of the acid sites. However, it will increase the number of acid sites, thus not inhibiting the adsorption of NH_3 . Acid sites comprise both Lewis (L) acid sites and Bronsted (B) acid sites, the determination of these two acid sites requires further analysis through mechanism calculations. For NO-TPD (Fig. 4c and f), there were obvious peaks belonging to bridged nitrite (253–262 °C) and bidentate nitrite (359–410 °C), indicating that the catalysts have a strong adsorption capacity for NO, and the intermediate substances are mainly bridged nitrite and bidentate nitrite [63,64]. Compared with the quasi-Mn-BTC without TEOS [21] (Fig. S11), the redox ability of the catalyst decreased by the regulated dual-ligand coordination, but their active sites were increased. The attenuation of the active site strength was compensated by the increased density of active site. The incorporation of a dual-ligand structure also facilitated the formation of Si-O-Mn bonds, which also resulted in an increased number of L acid sites. The increase in active sites can enhance the de- NO_x activity of the catalyst but not enhance the oxidation property of the catalyst, thereby inhibiting the oxidation of NH_3 and ensuring a favorable N_2 selectivity.

3.4. Reaction mechanism

In-situ diffuse reflectance infrared Fourier transform spectra

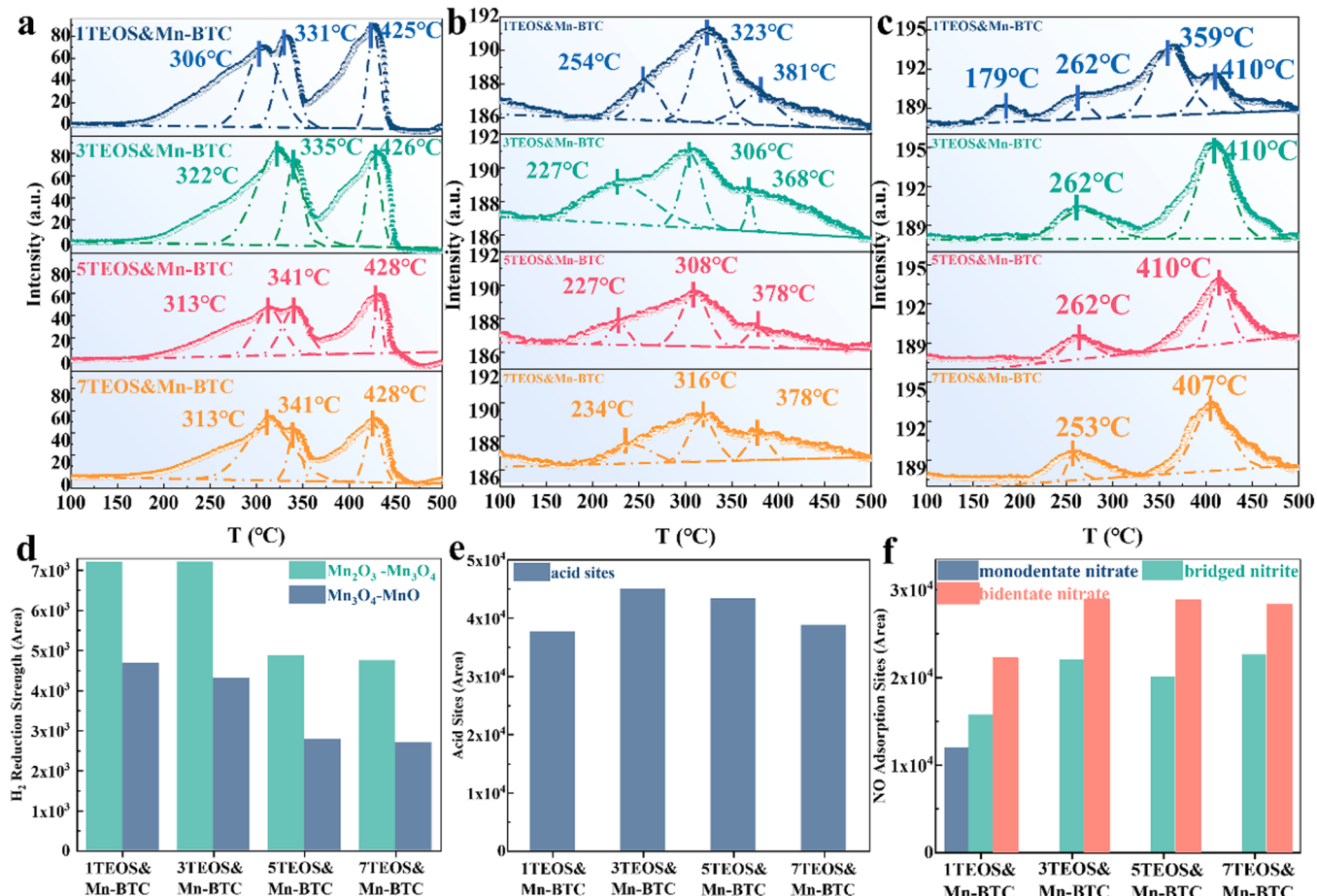


Fig. 4. $\text{H}_2\text{-TPR}$ (a and d), $\text{NH}_3\text{-TPD}$ (b and e), and NO-TPD (c and f) over $x\text{TEOS\&Mn-BTC}$.

(DRIFTS) were conducted on 3TEOS&Mn-BTC to explore the intermediates in the reaction process and the changes of the active site. After introducing NH_3 (Fig. 5a), many peaks appeared. The peaks at 3361 and 3241 cm^{-1} correspond to N-H stretching vibrations of NH_3 , while those at 1706 and 1461 cm^{-1} are attributed to NH_4^+ species on B

acid, peaks at 1591 and 1261 cm^{-1} are associated with NH_3 related to L acid, and the band at 966 cm^{-1} indicates weakly adsorbed NH_3 [65–68]. These findings substantiate the catalyst has a good adsorption capacity for NH_3 , aligning with the NH_3 -TPD results and the regulatory impact of dual-ligand competitive coordination. The effects of SO_2 (Fig. 5b) and

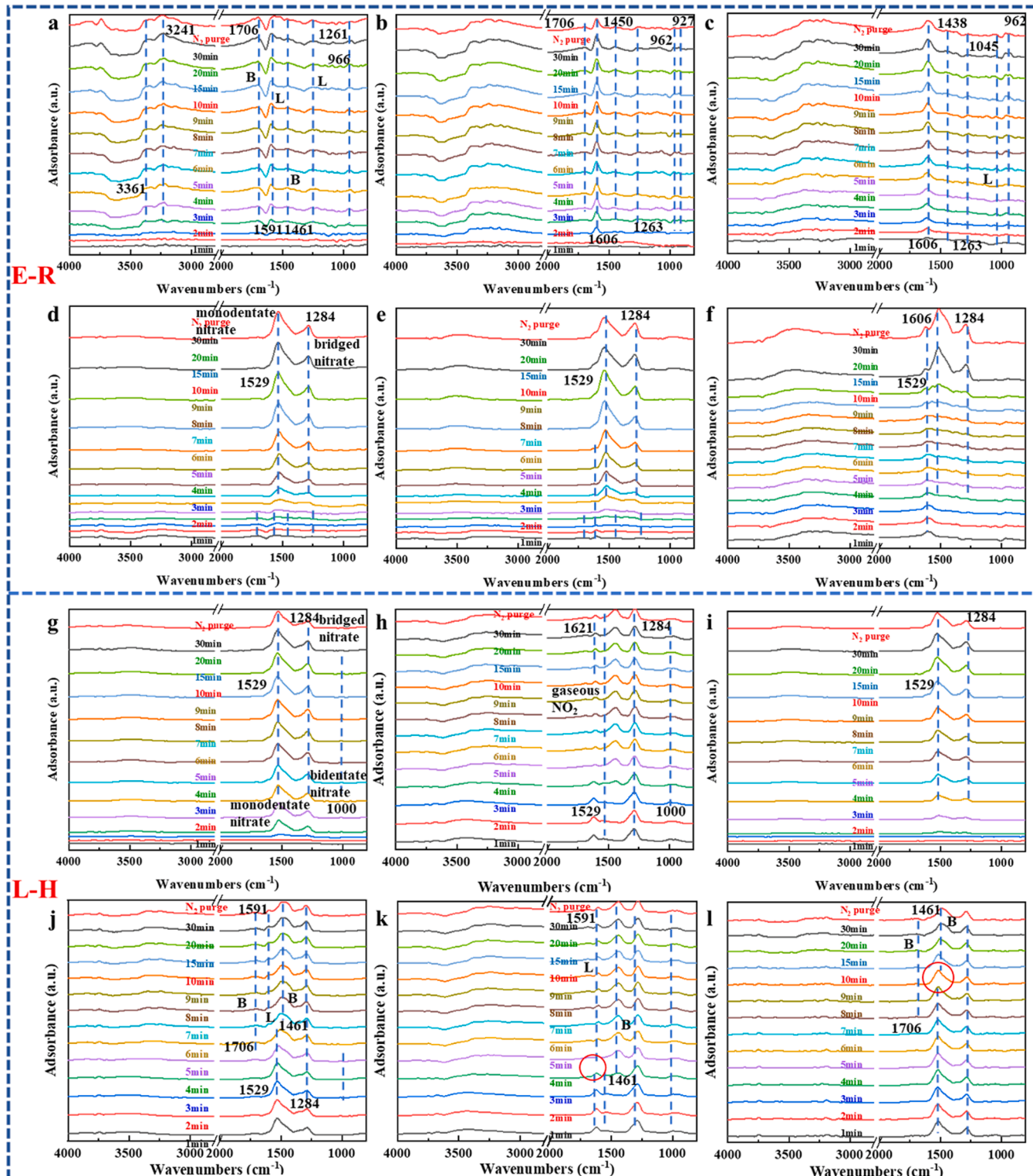


Fig. 5. Mechanism of NH_3 -SCR de- NO_x on 3TEOS&Mn-BTC: Dynamic changes of the in-situ DRIFTS in a flow of $\text{NO}+\text{O}_2$ (d) after pre-exposed to NH_3 (a) at 150 $^\circ\text{C}$; with the introduction of SO_2+O_2 (b) and H_2O (c) after pre-exposed to NH_3 ; with the introduction of SO_2+O_2 (e) and H_2O (f) in a flow of $\text{NO}+\text{O}_2$ after pre-exposed to NH_3 at 150 $^\circ\text{C}$; Dynamic changes of the in-situ DRIFTS in a flow of NH_3 (j) after pre-exposed to $\text{NO}+\text{O}_2$ (g) at 150 $^\circ\text{C}$; with the introduction of SO_2+O_2 (h) and H_2O (i) after pre-exposed to $\text{NO}+\text{O}_2$; with the introduction of SO_2+O_2 (k) and H_2O (l) in a flow of $\text{NO}+\text{O}_2$ after pre-exposed to NH_3 at 150 $^\circ\text{C}$.

H_2O (Fig. 5c) on NH_3 adsorption were also tested. Both SO_2 and H_2O attenuated NH_3 adsorption at the B and L acid sites, but the impact is small. Intriguingly, dual-ligand coordination induces the formation of Si-O-Mn bonds, leading to an increased abundance of L acid sites. Consequently, SO_2 exerts a diminished impact on the de- NO_x performance due to this fortification in the L acid site population.

The reaction of pre-adsorbed NH_3 with $\text{NO} + \text{O}_2$ was investigated (Fig. 5d). Upon introducing $\text{NO} + \text{O}_2$, the bands associated with adsorbed NH_3 species, B and L acid sites vanished, while peaks corresponding to bridged nitrate (1284 cm^{-1}) and monodentate nitrate (1529 cm^{-1}) emerged. This observation suggests that the reaction between free NO and adsorbed NH_3 occurs via the Eley-Rideal (E-R) mechanism [69,70]. To explore the impact of SO_2 (Fig. 5e) and H_2O (Fig. 5f) on the E-R reaction, it is evident that both SO_2 and H_2O impede the reaction of NO and NH_3 adsorbed on the B acid site. However, no peaks indicative of SO_2 , sulfate species, or H_2O appeared, indicating that SO_2 and H_2O do not disrupt the active site.

Upon the introduction of NO (Fig. 5g), monodentate nitrate (1529 cm^{-1}), bridged nitrate (1284 cm^{-1}) and bidentate nitrate (1000 cm^{-1}) swiftly emerged, indicating robust NO adsorption [70–74]. When SO_2 was introduced in (Fig. 5h), the peak corresponding to adsorbed NO_2 (1621 cm^{-1}) appeared, while the peak of monodentate nitrate gradually diminished. Thus, the presence of SO_2 induces the partial oxidation of adsorbed NO to NO_2 , potentially initiating the “Fast SCR” reaction ($2\text{NH}_3 + \text{NO} + \text{NO}_2 = 2\text{N}_2 + 3\text{H}_2\text{O}$) and enhancing the reaction rate. Upon the introduction of H_2O (Fig. 5i), the peaks associated with bidentate nitrate gradually vanished, with no discernible effect on the peaks of other intermediates.

The examination of the reaction involving pre-adsorbed $\text{NO} + \text{O}_2$ with NH_3 was also investigated (Fig. 5j). Upon the introduction of NH_3 , the bands assigned to monodentate nitrate and bidentate nitrate rapidly vanished. Simultaneously, the bands associated with B (1706 cm^{-1} and 1448 cm^{-1}) and L (1591 cm^{-1}) acid sites emerged, indicating that the reaction between adsorbed NO and NH_3 adheres to the Langmuir-Hinshelwood (L-H) mechanism [75,76]. Moreover, the intermediates

predominantly involved in the reaction are monodentate nitrate and bidentate nitrate. In the presence of SO_2 (Fig. 5k), the peaks corresponding to NO_2 and monodentate nitrate disappeared swiftly, while the peaks of B (1461 cm^{-1}) and L (1591 cm^{-1}) acid sites appeared, which suggests the initiation of the “Fast SCR” reaction. In the presence of H_2O (Fig. 5l), the peak of monodentate nitrate diminished gradually, and the peaks of B (1706 cm^{-1} and 1461 cm^{-1}) appeared, indicating a gradual occurrence of L-H reaction. However, peaks related to SO_2 , sulfate species and H_2O did not manifest. Therefore, these results signify that the de- NO_x reaction on 3TEOS&Mn-BTC involves two distinct reaction mechanisms, E-R and L-H. The transition states predominantly include monodentate nitrate, bridged nitrate, and bidentate nitrate. Additionally, the “Standard SCR” occurs in the E-R reaction ($4\text{NH}_3 + 4\text{NO} + \text{O}_2 = 4\text{N}_2 + 6\text{H}_2\text{O}$), while both “Standard SCR” and “Fast SCR” ($2\text{NH}_3 + \text{NO} + \text{NO}_2 = 2\text{N}_2 + 3\text{H}_2\text{O}$) manifest simultaneously in the L-H reaction.

3.5. Theoretical calculations

To further explore the electronic structure regulated by the dual-ligand coordination, we carried out density functional theory (DFT) calculations to clarify the structure of the active sites and transition states, charge transport, and formation of reaction intermediates (More details are presented in the Supporting Information, Section 4). Four clusters, including one cluster without Si (T) and three different dual-ligand coordination clusters (T1, T2 and T3), were selected to explore the structural features of xTEOS&Mn-BTC (Fig. 6).

Total density of states (TDOS) (Fig. 6a1-d1) show that, for T1 clusters, the TDOS peak decreases and the distribution of electrons near the Fermi level tends to be stable, resulting in enhanced electron delocalization for the transport of charges and the diffusion of adsorbed ions. This is one of the reasons for the increased performance, and the dual-ligand competition for coordination indeed modulates the electronic structure. The half-metallic nature of T1 structure is beneficial to the charge transfer and improvement of ion diffusion property of the catalyst, promoting the strong bonding between the adsorbate and the

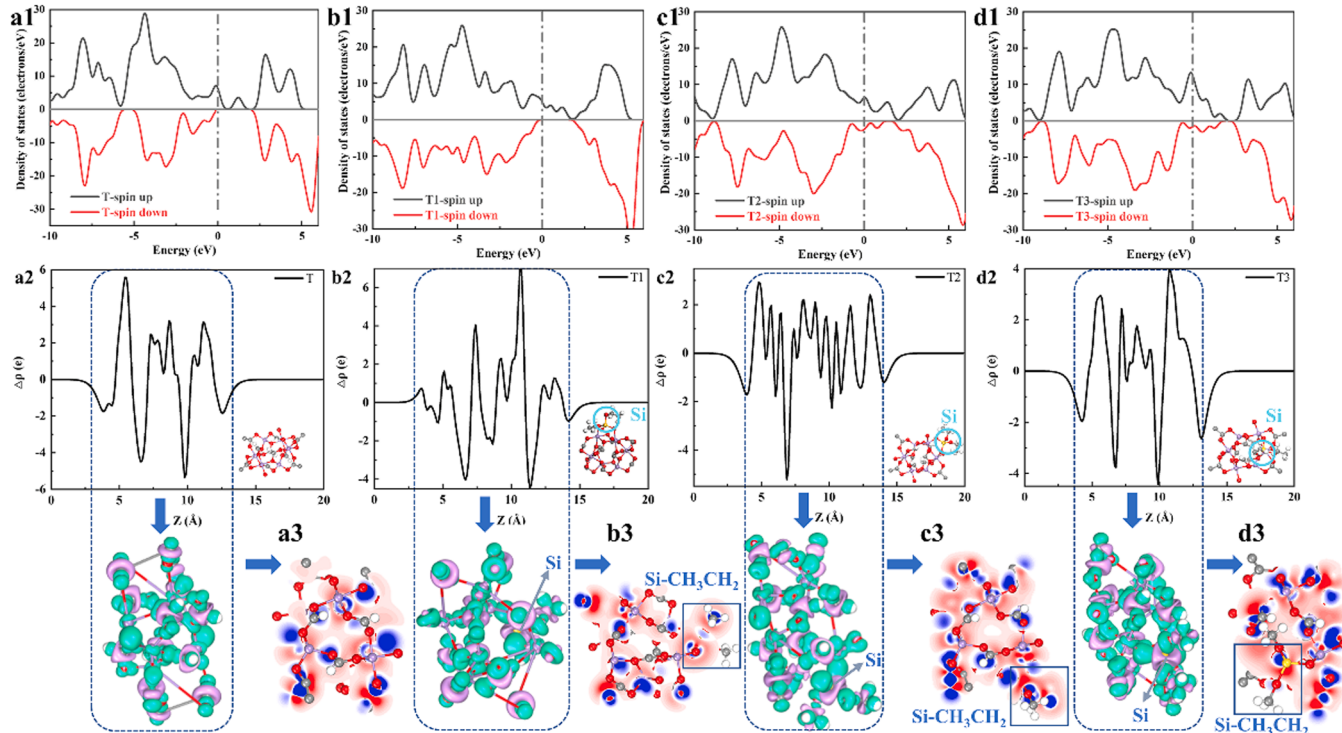


Fig. 6. Electronic properties: The TDOS (1), EDD (2) and slice electron density distribution (3) of T (a), T1 (b), T2 (c) and T3 (d) clusters. The Fermi level is set at 0 eV.

reaction center. For T2 and T3 clusters, the introduction of TEOS led to a transition from half-metallic to metallic, and they may not be as active as the T1 cluster.

The electron density differences (EDD) of the four clusters were further explored. From the plane-averaged differential density along the Z-axis of the periodic structure ($+\Delta\rho/\Delta\rho$ represents the gain/loss of electrons, Fig. 6 a2-d2), it is found that the accumulation of net charge during electron transfer results in the formation of a built-in electric field (green/purple is the gain/loss of electrons). The built-in electric field induces charge redistribution, accelerates charge transport, and creates additional charge transport channels on the surface, contributing to faster charge transfer kinetics. From the slices of the same position of the clusters, it can be seen that the arrangement of electron cloud around the atoms has changed significantly (blue/red is the gain/loss of electron, Fig. 6 a3-d3), implying the different coordination of the two ligands cause the redistribution of the cluster electrons.

Based on three different binding modes of two ligands, twelve initial adsorption configurations of NH_3 (Fig. S12) and eighteen initial adsorption configurations of NO were established (Fig. S13). From the

adsorption energies of NH_3 (Fig. S14a) and NO (Fig. S14b), we can know that NH_3 adsorption on the L acid site is stronger than that on the B acid site. The most stable configuration for NH_3 adsorption on the L acid site is T1- $\text{NH}_3\text{-}2$ and the most stable adsorption of NH_3 on the B acid site is T3- $\text{NH}_3\text{-}1$. The adsorption of NO on T1 cluster is the most stable, especially in the two configurations of T1-NO-3 and T1-NO-4. Therefore, the adsorption of NH_3 and NO basically occurs on the T1 cluster, which is consistent with the structural electronic properties.

On the T1 cluster, the initial adsorption configuration of NH_3 is more stable than that of NO. Since NO is weakly adsorbed on T2 and T3 clusters, and NO-TPD and in-situ DRIFTS confirm the catalyst has a strong adsorption capacity for NO, the structure of catalyst for NO is mainly T1 cluster. Therefore, we selected the adsorption configurations of T1- $\text{NH}_3\text{-}2$, T3- $\text{NH}_3\text{-}1$, T1-NO-3 and T1-NO-4 to further explore the adsorption of NH_3 (Fig. 7a-b) and NO (Fig. 7c-d). The results of the plane-averaged differential density along the Z-axis imply that there is an obvious net charge accumulation between the adsorbate and the active site, and that the generation of the built-in electric field promotes the adsorption of NH_3 and NO. The charge distribution shown in the

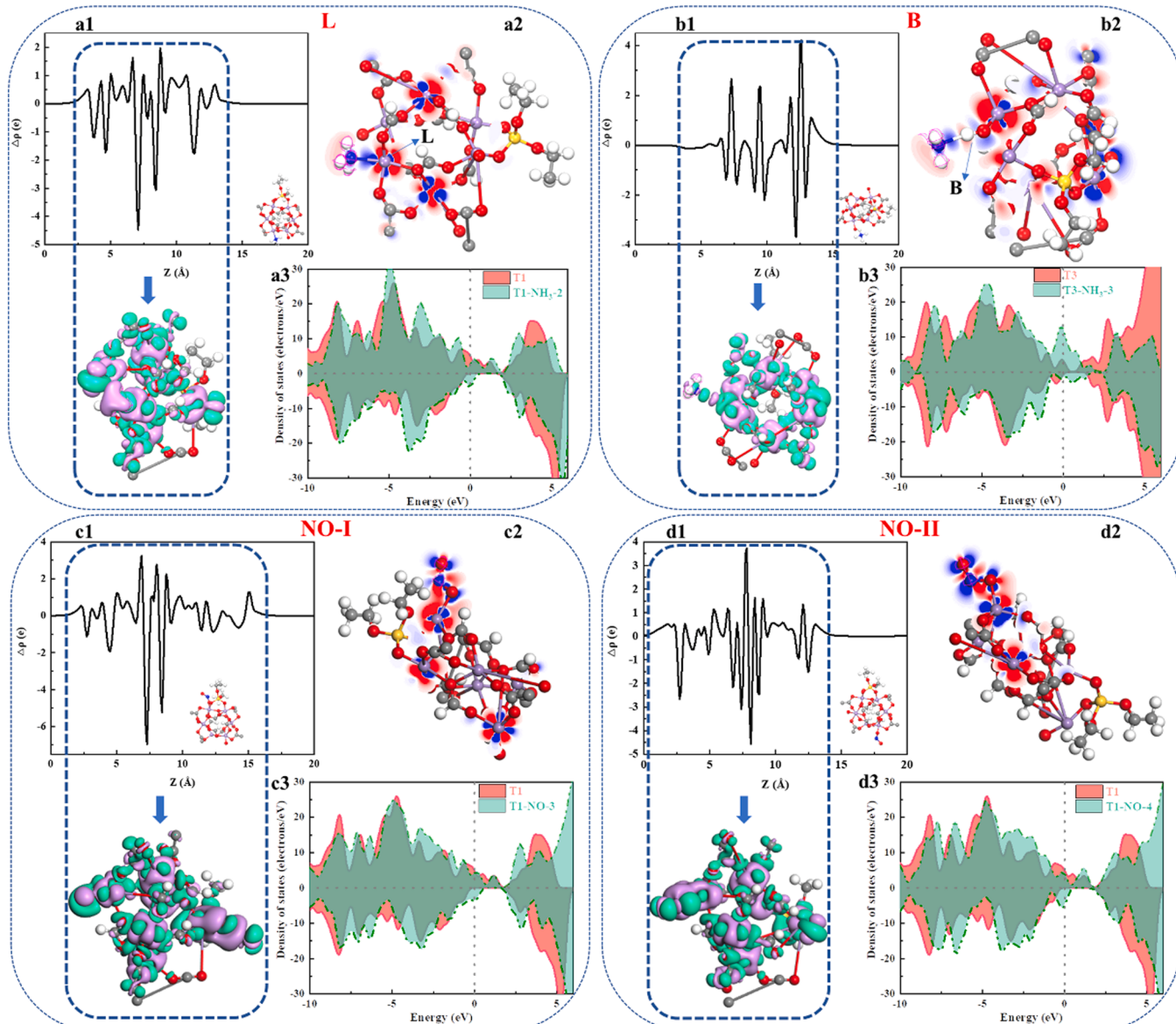


Fig. 7. Electronic properties: The EDD (1), slice electron density distribution (2) and TDOS (3) of the most stable configuration for adsorption, including NH_3 on T1- $\text{NH}_3\text{-}2$ (a) and T3- $\text{NH}_3\text{-}1$ (b), NO on T1-NO-3 (c) and T1-NO-4 (d). The Fermi level is set at 0 eV.

slices (Fig. 7 a2, b2, c2 and d2) indicates there is an obvious charge transfer near the adsorption site. Therefore, under the dual-ligand coordination with BTC and TEOS, compared to a single BTC ligand, the adsorption of the catalyst for NH_3 and NO is significantly improved [21].

By comparing the TDOS of the structure before and after adsorption, it is found that the TDOS of the structure after the adsorption shifts positively, indicating that the adsorption has occurred and hole carriers are generated to promote the generation of the built-in electric field. Based on the above results, the adsorption structures of NH_3 are determined to be T1- NH_3 -2 (L) and T3- NH_3 -1 (B). According to the principle of the lowest energy path and the L-H reaction mechanism, the adsorption configuration of NO is selected to be adsorbed near NH_3 , as T1-NO-4. Considering that T1 is the main structure, four initial configurations for SO_2 adsorption (Fig. S15a) and two initial configurations for H_2O adsorption (Fig. S15b) were then established on the basis of T1 structure and used to further analyze the SO_2 and H_2O tolerance of the catalyst. The adsorption energies of SO_2 (Fig. S15c) and H_2O (Fig. S15d) on the catalyst are both small to only produce weak adsorption. SO_2 and H_2O occupy a part of the B acid sites, thereby preventing the adsorption of NH_3 on the B sites. This is also the reason that the de- NO_x performance of the catalyst decreased slightly at the co-presence of SO_2 and H_2O .

Based on the above experimental and computational results, we could establish the whole reaction process (Fig. 8a) and analyze the L-H reaction route including the “Fast SCR” (Fig. 8b) and E-R reaction route (Fig. 8c) on the optimized T1 cluster. For both E-R and L-H, the pivotal step involves the reaction of NH_2 with NO, leading to the formation of NH_2NO , subsequently transforming into HNNOH . For L-H reaction, the former reaction exhibits an energy barrier of 0.45 eV, while the latter reaction entails an energy barrier of 0.47 eV. For E-R reaction, the

energy barriers of the two reactions are 0.40 and 0.45 eV, respectively. Notably, all these energy barriers are lower than those observed for the single-ligand quasi-Mn-BTC without TEOS [21], suggesting that dual-ligand coordination effectively reduces the energy barrier for the reaction, consequently expediting the reaction rate and enhancing the de- NO_x activity of the catalyst with two ligands. What is more, for the reaction occurring at the L acid site, the energy barrier of the E-R reaction mechanism is lower than that of the L-H, rendering the E-R reaction more likely to occur.

Although the energy barrier of the “Fast SCR” reaction at the B acid site in the L-H reaction is comparable to that of the “Standard SCR” reaction, the “Fast SCR” reaction is more likely to occur due to its greater exothermic nature and fewer reaction processes. The energy barrier of E-R reaction at the B acid site is higher than that of L-H reaction. Therefore, the SCR reaction at the B acid site on 3TEOS&Mn-BTC is more prone to proceed via the “Fast SCR” pathway in the L-H mechanism.

Additionally, the formation of N_2O was analyzed to investigate N_2 selectivity (Fig. 8d). In the first reaction pathway for N_2O generating, the overall reaction is endothermic, despite a lower energy barrier than that of the SCR reaction. Therefore, the reaction is challenging to occur unless the temperature is very high, leading to a reduction in N_2 selectivity at elevated temperatures. In the second reaction pathway, the energy barrier (TS16) for the reaction of NO and NH_3 to generate N_2O is higher than that of the SCR reaction to generate NH_3NO_2 . Hence, the SCR reaction will prevail, suppressing the formation of N_2O .

4. Conclusions

We have meticulously synthesized x TEOS&Mn-BTC hollow sea-

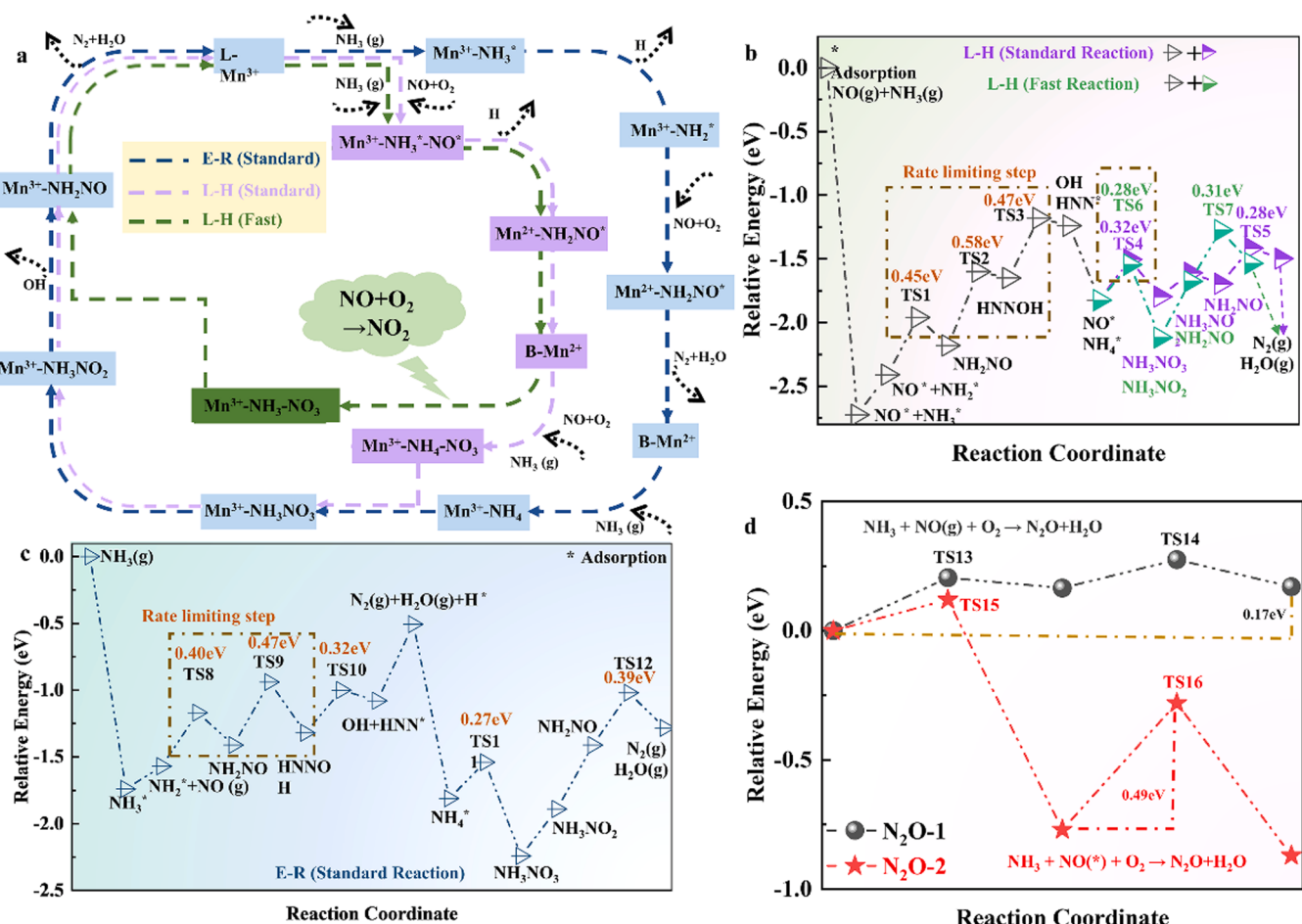


Fig. 8. Reaction mechanism over 3TEOS&Mn-BTC (a); DFT calculations for reaction pathways of L-H (b) and E-R (c) and the reaction pathway of N_2O formation (d).

urchin-like microspheres by two-ligand coordination. 3TEOS&Mn-BTC exhibited NO conversion of above 90% at 60–330 °C at the GHSV of 36,000 h⁻¹. It also exhibited the best H₂O tolerance of only 1–2% NO conversion decrease with 6% H₂O, SO₂ tolerance of 5–6% NO conversion decrease with 100 ppm SO₂, and an increased N₂ selectivity (above 90%, 60–270 °C). The dual ligands engender a built-in electric field to promote the redistribution and contribute to faster charge transfer kinetics, and highlighting an increased exposure of defects. Furthermore, the Si-O-Mn coordination structure is also formed with electron-metal-carrier interaction that can generate more L acid site and promote the thermal stability. In addition to the reason of electronic regulation mechanism, another profound observation that is conducive to improving activity and breaking seesaw effect is the formation of hollow sea-urchin-like microspheres with a void confinement effect. This hollow sea-urchin-like microspheres greatly shortens the mass transfer distance, realizes the amplification of the active site, safeguards intermediates, reduces the mass transfer loss, and helps the generation of hierarchical porous structure. Besides, dual-ligand coordination indeed reduces the energy barrier for the reaction and facilitated partitioning responses, the E-R reaction more likely to occur at the L acid site and the “Fast SCR” reaction of L-H is more likely to proceed at the B acid site, which promotes the activity while inhibiting the occurrence of side reactions. This research sheds light on the multifaceted potentials of dual-ligand MOF designs and their application for breaking the seesaw effect between catalytic activity and N₂ selectivity.

CRediT authorship contribution statement

Bo Qin: Visualization. **Yufei Jia:** Validation. **Chi He:** Project administration, Formal analysis. **Yu Chen:** Resources. **Shaobin Wang:** Writing – review & editing, Formal analysis. **Xinya Zhou:** Data curation. **Yonghong Cheng:** Project administration. **Jian-Wen Shi:** Writing – review & editing, Supervision, Funding acquisition, Conceptualization. **Yimeng Zhang:** Visualization. **Kunli Song:** Writing – original draft, Investigation. **Liang Liang:** Software. **Dandan Ma:** Formal analysis. **Jun Li:** Formal analysis. **Yuwei Gui:** Formal analysis.

Declaration of Competing Interest

The authors declare that they have no known competing financial interests or personal relationships that could have appeared to influence the work reported in this paper.

Data Availability

Data will be made available on request.

Acknowledgements

This work was supported by the National Natural Science Foundation of China (21972110), the Fundamental Research Funds for the Central Universities (xtr062023001), and the State Key Laboratory of Electrical Insulation and Power Equipment (EIPE23315). SEM and TEM were measured at the Analysis and Test Center of Xi'an Jiaotong University, and we thank Mr. Kaiyu Guo and Mr. Jiaqi Han for their assistance in the SEM, Miss Jia Shui and Mr. Chao Li for their assistance in the TEM.

Supplemental information

Detailed experimental procedures and characterization methods; Detailed experimental setup for catalytic testing; Detailed in-situ DRIFTS and DFT calculations methods; TGA experiments; PXRD experiments; Raman experiments; SEM and TEM experiments; De-NO_x activity at high GHSV, and H₂O and SO₂ co-tolerance experiments; Crystal structure and adsorption configurations analysis; N₂ adsorption-desorption experiments; XPS experiments; Comparison of catalysts

performance.

Appendix A. Supporting information

Supplementary data associated with this article can be found in the online version at doi:10.1016/j.apcatb.2024.124131.

References

- [1] Y. Shan, G. He, J. Du, Y. Sun, Z. Liu, Y. Fu, F. Liu, X. Shi, Y. Yu, H. He, Strikingly distinctive NH₃-SCR behavior over Cu-SSZ-13 in the presence of NO₂, *Nat. Commun.* 13 (2022) 4606.
- [2] W. Qu, X. Liu, J. Chen, Y. Dong, X. Tang, Y. Chen, Single-atom catalysts reveal the dinuclear characteristic of active sites in NO selective reduction with NH₃, *Nat. Commun.* 11 (2020) 1532.
- [3] L.E. Gevers, L.R. Enakonda, A. Shahid, S. Ould-Chikh, C.I. Silva, P.P. Paalanen, A. Aguilar-Tapia, J.-L. Hazemann, M.N. Hedhili, F. Wen, Unraveling the structure and role of Mn and Ce for NO_x reduction in application-relevant catalysts, *Nat. Commun.* 13 (2022) 2960.
- [4] X. Liu, P. Jiang, Y. Chen, Y. Wang, Q. Ding, Z. Sui, H. Chen, Z. Shen, X. Wu, A basic comprehensive study on synergistic effects among the metal oxides in CeO₂-WO₃/TiO₂ NH₃-SCR catalyst, *Chem. Eng. J.* 421 (2021) 127833.
- [5] A. Marberger, A.W. Petrov, P. Steiger, M. Elsener, O. Kröcher, M. Nachtegaal, D. Ferri, Time-resolved copper speciation during selective catalytic reduction of NO on Cu-SSZ-13, *Nat. Catal.* 1 (2018) 221–227.
- [6] S.H. Krishna, A. Goswami, Y. Wang, C.B. Jones, D.P. Dean, J.T. Miller, W. F. Schneider, R. Gounder, Influence of framework Al density in chabazite zeolites on copper ion mobility and reactivity during NO x selective catalytic reduction with NH₃, *Nat. Catal.* 6 (2023) 276–285.
- [7] C.X. Chen, Y.Y. Xiong, X. Zhong, P.C. Lan, Z.W. Wei, H. Pan, P.Y. Su, Y. Song, Y. F. Chen, A. Nafady, Enhancing photocatalytic hydrogen production via the construction of robust multivariate Ti-MOF/COF composites, *Angew. Chem. Int. Ed.* 134 (2022) e202114071.
- [8] A. Ghosh, S. Karmakar, F.A. Rahimi, R.S. Roy, S. Nath, U.K. Gautam, T.K. Maji, Confinement matters: Stabilization of CdS nanoparticles inside a postmodified MOF toward photocatalytic hydrogen evolution, *ACS Appl. Mater. Interfaces* 14 (2022) 25220–25231.
- [9] S. Mao, J.-W. Shi, G. Sun, Y. Zhang, D. Ma, K. Song, Y. Lv, J. Zhou, H. Wang, Y. Cheng, PdS quantum dots as a hole attractor encapsulated into the MOF@Cd_{0.5}Zn_{0.5}S heterostructure for boosting photocatalytic hydrogen evolution under visible light, *ACS Appl. Mater. Interfaces* 14 (2022) 48770–48779.
- [10] R. Shimoni, Z. Shi, S. Binyamin, Y. Yang, I. Liberman, R. Ifraimov, S. Mukhopadhyay, L. Zhang, I. Hod, Electrostatic secondary-sphere interactions that facilitate rapid and selective electrocatalytic CO₂ reduction in a Fe-porphyrin-based metal–organic framework, *Angew. Chem. Int. Ed.* 134 (2022) e202206085.
- [11] H.-J. Zhu, M. Lu, Y.-R. Wang, S.-J. Yao, M. Zhang, Y.-H. Kan, J. Liu, Y. Chen, S.-L. Li, Y.-Q. Lan, Efficient electron transmission in covalent organic framework nanosheets for highly active electrocatalytic carbon dioxide reduction, *Nat. Commun.* 11 (2020) 497.
- [12] Y. Xue, G. Zhao, R. Yang, F. Chu, J. Chen, L. Wang, X. Huang, 2D metal–organic framework-based materials for electrocatalytic, photocatalytic and thermocatalytic applications, *Nanoscale* 13 (2021) 3911–3936.
- [13] G. Qin, J. Zheng, Y. Li, Y. Yang, X. Liu, X. Han, Z. Huang, Tailor the crystal planes of MIL-101 (Fe) derivatives to enhance the activity of SCR reaction at medium and low temperature, *J. Colloid Interface Sci.* 615 (2022) 432–444.
- [14] K. Song, K. Guo, Y. Lv, D. Ma, Y. Cheng, J.-W. Shi, Rational regulation of reducibility and acid site on Mn–Fe–BTC to achieve high low-temperature catalytic denitration performance, *ACS Appl. Mater. Interfaces* (2023).
- [15] H. Li, H. Gong, Z. Jin, Phosphorus modified Ni-MOF-74/BiVO₄ S-scheme heterojunction for enhanced photocatalytic hydrogen evolution, *Appl. Catal. B* 307 (2022) 121166.
- [16] P.S. Pauletti, T.J. Bandosz, Activated carbon versus metal–organic frameworks: A review of their PFAS adsorption performance, *J. Hazard. Mater.* 425 (2022) 127810.
- [17] J. Qin, Y. Pei, Y. Zheng, D. Ye, Y. Hu, Fe-MOF derivative photocatalyst with advanced oxygen reduction capacity for indoor pollutants removal, *Appl. Catal. B* 325 (2023) 122346.
- [18] X. Zhang, B. Shen, X. Zhang, F. Wang, G. Chi, M. Si, A comparative study of manganese–cerium doped metal–organic frameworks prepared via impregnation and in situ methods in the selective catalytic reduction of NO, *RSC Adv.* 7 (2017) 5928–5936.
- [19] Y. Yu, C. Chen, C. He, J. Miao, J. Chen, In situ growth synthesis of CuO@Cu-MOFs core-shell materials as novel low-temperature NH₃-SCR catalysts, *ChemCatChem* 11 (2019) 979–984.
- [20] Z. Liu, G. Sun, C. Chen, K. Sun, L. Zeng, L. Yang, Y. Chen, W. Wang, B. Liu, Y. Lu, Fe-doped Mn₃O₄ spinel nanoparticles with highly exposed FeO_x–Mn₃O₄ sites for efficient selective catalytic reduction (SCR) of NO with ammonia at low temperatures, *ACS Catal.* 10 (2020) 6803–6809.
- [21] K. Song, K. Guo, S. Mao, D. Ma, Y. Lv, C. He, H. Wang, Y. Cheng, J.-W. Shi, Insight into the origin of excellent SO₂ tolerance and de-NO_x performance of quasi-Mn-BTC in the low-temperature catalytic reduction of nitrogen oxide, *ACS Catal.* 13 (2023) 5020–5032.

- [22] X. Yang, K. Liu, X. Han, J. Xu, M. Bian, D. Zheng, H. Xie, Y. Zhang, X. Yang, Transformation of waste battery cathode material LiMn_2O_4 into efficient ultra-low temperature $\text{NH}_3\text{-SCR}$ catalyst: Proton exchange synergistic vanadium modification, *J. Hazard. Mater.* 459 (2023) 132209.
- [23] Z. Gao, R. Yang, Z. Wang, W. Liu, M. Sun, C. Zhang, L. Yu, Promotion effect of iron on activity and N_2 selectivity of Mn/Ce catalysts in the $\text{NH}_3\text{-SCR}$ reaction, *Ind. Eng. Chem. Res.* 62 (2023) 8673–8683.
- [24] M. Rubio-Martinez, C. Avci-Camur, A.W. Thornton, I. Imaz, D. Maspoch, M.R. Hill, New synthetic routes towards MOF production at scale, *Chem. Soc. Rev.* 46 (2017) 3453–3480.
- [25] R. Freund, O. Zaremba, G. Arnauts, R. Ameloot, G. Skorupskii, M. Dincă, A. Bavykina, J. Gascon, A. Ejsmont, J. Goscianska, The current status of MOF and COF applications, *Angew. Chem. Int. Ed.* 60 (2021) 23975–24001.
- [26] B.F. Rivadeneira-Mendoza, O.A. Estrela Filho, K.J. Fernández-Andrade, F. Curbelo, F.F. da Silva, R. Luque, J.M. Rodríguez-Díaz, MOF@ biomass hybrids: Trends on advanced functional materials for adsorption, *Environ. Res.* 216 (2023) 114424.
- [27] A.-Q. Wu, W.-Q. Wang, H.-B. Zhan, L.-A. Cao, X.-L. Ye, J.-J. Zheng, P.N. Kumar, K. Chiranjeevulu, W.-H. Deng, G.-E. Wang, Layer-by-layer assembled dual-ligand conductive MOF nano-films with modulated chemiresistive sensitivity and selectivity, *Nano Res.* 14 (2021) 438–443.
- [28] M.S. Yao, J.J. Zheng, A.Q. Wu, G. Xu, S.S. Nagarkar, G. Zhang, M. Tsujimoto, S. Sakaki, S. Horike, K. Otake, A dual-ligand porous coordination polymer chemiresistor with modulated conductivity and porosity, *Angew. Chem. Int. Ed.* 59 (2020) 172–176.
- [29] G. De, B. Karmakar, D. Ganguli, Hydrolysis-condensation reactions of TEOS in the presence of acetic acid leading to the generation of glass-like silica microspheres in solution at room temperature, *J. Mater. Chem.* 10 (2000) 2289–2293.
- [30] C.J. Brinker, Hydrolysis and condensation of silicates: Effects on structure, *J. Non Cryst. Solids* 100 (1988) 31–50.
- [31] M. Van Bommel, T. Bernards, A. Boonstra, The influence of the addition of alkyl-substituted ethoxysilane on the hydrolysis—condensation process of TEOS, *J. Non Cryst. Solids* 128 (1991) 231–242.
- [32] D. Nagao, T. Satoh, M. Konno, A generalized model for describing particle formation in the synthesis of monodisperse oxide particles based on the hydrolysis and condensation of tetraethyl orthosilicate, *J. Colloid Interface Sci.* 232 (2000) 102–110.
- [33] F.C. Tompkins, Superficial chemistry and solid imperfections, *Nature* 186 (1960) 3–6.
- [34] N. Tsumori, L. Chen, Q. Wang, Q.-L. Zhu, M. Kitto, Q. Xu, Quasi-MOF: exposing inorganic nodes to guest metal nanoparticles for drastically enhanced catalytic activity, *Chem* 4 (2018) 845–856.
- [35] L. Fan, F. Zhao, Z. Huang, B. Chen, S.-F. Zhou, G. Zhan, Partial deligation of M/Ce-BTC nanorods ($M = \text{Au, Cu, au-cu}$) with “Quasi-MOF” structures towards improving catalytic activity and stability, *Appl. Catal. A-Gen.* 572 (2019) 34–43.
- [36] L. Zhang, A. Eisenberg, Multiple morphologies of “crew-cut” aggregates of polystyrene-b-poly (acrylic acid) block copolymers, *Science* 268 (1995) 1728–1731.
- [37] Y. Mai, A. Eisenberg, Self-assembly of block copolymers, *Chem. Soc. Rev.* 41 (2012) 5695–5955.
- [38] D.E. Discher, A. Eisenberg, Polymer vesicles, *Science* 297 (2002) 967–973.
- [39] C.M. Parlett, K. Wilson, A.F. Lee, Hierarchical porous materials: catalytic applications, *Chem. Soc. Rev.* 42 (2013) 3876–3893.
- [40] Z. Hu, G. Chen, Novel nanocomposite hydrogels consisting of layered double hydroxide with ultrahigh tensility and hierarchical porous structure at low inorganic content, *Adv. Mater. (Weinh., Ger.)* 26 (2014) 5950–5956.
- [41] Y. Zhang, S. Fan, X. Li, L. Wang, Z. Yin, P. Wang, M.O. Tadé, S. Liu, Sea-urchin-like carbon nanospheres for electrocatalytic dechlorination of 1, 2-dichloroethane, *ACS Appl. Nano Mater.* 4 (2021) 13090–13098.
- [42] C. Bai, S. Fan, X. Li, Z. Niu, J. Wang, Z. Liu, D. Zhang, Hollow $\text{Cu}_2\text{O}@\text{CoMn}_2\text{O}_4$ nanoreactors for electrochemical NO reduction to NH_3 : Elucidating the void-confinement effects on intermediates, *Adv. Funct. Mater.* 32 (2022) 2205569.
- [43] J. Liu, X. Meng, J. Xie, B. Liu, B. Tang, R. Wang, C. Wang, P. Gu, Y. Song, S. Huo, Dual active sites engineering on sea urchin-like CoNiS hollow nanosphere for stabilizing oxygen electrocatalysis via a template-free vulcanization strategy, *Adv. Funct. Mater.* (2023) 2300579.
- [44] C. Buttersack, Modeling of type IV and V sigmoidal adsorption isotherms, *Phys. Chem. Chem. Phys.* 21 (2019) 5614–5626.
- [45] M. Wang, S. Ren, Y. Jiang, B. Su, Z. Chen, W. Liu, J. Yang, L. Chen, Insights into co-doping effect of Sm and Fe on anti-Pb poisoning of Mn-Ce/AC catalyst for low-temperature SCR of NO with NH_3 , *Fuel* 319 (2022) 123763.
- [46] C. Peng, R. Yan, H. Peng, Y. Mi, J. Liang, W. Liu, X. Wang, G. Song, P. Wu, F. Liu, One-pot synthesis of layered mesoporous ZSM-5 plus Cu ion-exchange: Enhanced $\text{NH}_3\text{-SCR}$ performance on Cu-ZSM-5 with hierarchical pore structures, *J. Hazard. Mater.* 385 (2020) 121593.
- [47] W. Miao, Y. Zhang, H. Li, Z. Zhang, L. Li, Z. Yu, W. Zhang, ZIF-8/ZIF-67-derived 3D amorphous carbon-encapsulated CoS/NCNTs supported on CoS-coated carbon nanofibers as an advanced potassium-ion battery anode, *J. Mater. Chem. A* 7 (2019) 5504–5512.
- [48] X. Zhao, X. Yang, M. Wang, S. Hwang, S. Karakalos, M. Chen, Z. Qiao, L. Wang, B. Liu, Q. Ma, Single-iron site catalysts with self-assembled dual-size architecture and hierarchical porosity for proton-exchange membrane fuel cells, *Appl. Catal. B* 279 (2020) 119400.
- [49] J. Lu, X. Wang, H. Li, S. Shi, W. Yang, Y. Lu, S. Shao, Q. Ye, Molecular insights into the methane adsorption capacity of coal under microwave irradiation based on solid-state ^{13}C NMR and XPS, *Fuel* 339 (2023) 127484.
- [50] T. Si, L. Wang, H. Zhang, X. Lu, X. Liang, S. Wang, Y. Guo, Core-shell MOFs-based composites of defect-functionalized for mixed-mode chromatographic separation, *J. Chromatogr. A* 1671 (2022) 463011.
- [51] M. Wang, Y. Zi, J. Zhu, W. Huang, Z. Zhang, H. Zhang, Construction of super-hydrophobic PDMS@ MOF@ Cu mesh for reduced drag, anti-fouling and self-cleaning towards marine vehicle applications, *Chem. Eng. J.* 417 (2021) 129265.
- [52] P. Wang, S. Bater, L. Zhang, M. Ascherl, J. Craig Jr, XPS investigation of electron beam effects on a trimethylsilane dosed Si (100) surface, *Appl. Surf. Sci.* 90 (1995) 413–417.
- [53] N. Huang, D. Wang, Q. Xiong, B. Yang, XPS study of hydrogen permeation effect on SiC-C films, *Nucl. Instrum. Meth. B* 207 (2003) 395–401.
- [54] D. Ma, W. Liu, Y. Huang, D. Xia, Q. Lian, C. He, Enhanced catalytic ozonation for eliminating CH_3SH via stable and circular electronic metal-support interactions of Si-O-Mn bonds with low Mn loading, *Environ. Sci. Technol.* 56 (2022) 3678–3688.
- [55] B. Zhang, L. Zhou, M. Qi, Z. Li, J. Han, K. Li, Y. Zhang, F. Dehghani, R. Liu, J. Yun, Outstanding stability and enhanced catalytic activity for toluene oxidation by Si-O-Mn interaction over $\text{MnO}_x/\text{SiO}_2$, *Ind. Eng. Chem. Res.* 61 (2022) 1044–1055.
- [56] X. Han, Y. Hong, Y. Ma, W. Lu, J. Li, L. Lin, A.M. Sheveleva, F. Tuna, E.J. McInnes, C. Dejoie, Adsorption of nitrogen dioxide in a redox-active vanadium metal-organic framework material, *J. Am. Chem. Soc.* 142 (2020) 15235–15239.
- [57] J. Yang, S. Hu, Y. Fang, S. Hoang, L. Li, W. Yang, Z. Liang, J. Wu, J. Hu, W. Xiao, Oxygen vacancy promoted O_2 activation over perovskite oxide for low-temperature CO oxidation, *ACS Catal.* 9 (2019) 9751–9763.
- [58] M.E.C. Pascuzzi, J.P. Hofmann, E.J. Hensen, Promoting oxygen evolution of IrO_2 in acid electrolyte by Mn, *Electrochim. Acta* 366 (2021) 137448.
- [59] M. Huynh, C. Shi, S.J. Billinge, D.G. Nocera, Nature of activated manganese oxide for oxygen evolution, *J. Am. Chem. Soc.* 137 (2015) 14887–14904.
- [60] Y. Li, G. Li, Y. Zou, W. Liu, H. Zhang, S. Lu, Z. Li, S. Zhang, H. Peng, Unveiling the remarkable deNO_x performance of MnMoVO_x catalysts via dual regulation of the redox and acid sites, *Appl. Catal. B* 344 (2024) 123612.
- [61] J. Li, C. Zhang, Q. Li, T. Gao, S. Yu, P. Tan, Q. Fang, G. Chen, Promoting mechanism of SO_2 resistance performance by anatase $\text{TiO}_2\{0\ 0\ 1\}$ facets on Mn-Ce/TiO₂ catalysts during $\text{NH}_3\text{-SCR}$ reaction, *Chem. Eng. Sci.* 251 (2022) 117438.
- [62] C. Niu, B. Wang, Y. Xing, W. Su, C. He, L. Xiao, Y. Xu, S. Zhao, Y. Cheng, J.-W. Shi, Thulium modified $\text{MnO}_x/\text{TiO}_2$ catalyst for the low-temperature selective catalytic reduction of NO with ammonia, *J. Clean. Prod.* 290 (2021) 125858.
- [63] H. Xue, X. Guo, T. Meng, Q. Guo, D. Mao, S. Wang, Cu-ZSM-5 catalyst impregnated with Mn-Co oxide for the selected catalytic reduction of NO: physicochemical property-catalytic activity relationship and in situ DRIFTS study for the reaction mechanism, *ACS Catal.* 11 (2021) 7702–7718.
- [64] D. Meng, W. Zhan, Y. Guo, Y. Guo, L. Wang, G. Lu, A highly effective catalyst of Sm- MnO_x for the $\text{NH}_3\text{-SCR}$ of NO_x at low temperature: promotional role of Sm and its catalytic performance, *ACS Catal.* 5 (2015) 5973–5983.
- [65] Z. Zhang, R. Li, M. Wang, Y. Li, Y. Tong, P. Yang, Y. Zhu, Two steps synthesis of CeTiO_x oxides nanotube catalyst: Enhanced activity, resistance of SO_2 and H_2O for low-temperature $\text{NH}_3\text{-SCR}$ of NO_x , *Appl. Catal. B* 282 (2021) 119542.
- [66] Q. Yan, S. Chen, C. Zhang, Q. Wang, B. Louis, Synthesis and catalytic performance of $\text{Cu}_1\text{Mn}_0.5\text{Ti}_{0.5}\text{O}_x$ mixed oxide as low-temperature $\text{NH}_3\text{-SCR}$ catalyst with enhanced SO_2 resistance, *Appl. Catal. B* 238 (2018) 236–247.
- [67] D. Wang, Y. Peng, S.-c. Xiong, B. Li, L.-n. Gan, C.-m. Lu, J.-j. Chen, Y.-l. Ma, J.-h. Li, De-reducibility mechanism of titanium on maghemite catalysts for the SCR reaction: An in situ DRIFTS and quantitative kinetics study, *Appl. Catal. B* 221 (2018) 556–564.
- [68] S. Xie, Q. Qin, H. Liu, L. Jin, X. Wei, J. Liu, X. Liu, Y. Yao, L. Dong, B. Li, MOF-74-M ($M = \text{Mn, Co, Ni, Zn, MnCo, MnNi, and MnZn}$) for low-temperature $\text{NH}_3\text{-SCR}$ and in situ DRIFTS study reaction mechanism, *ACS Appl. Mater. Interfaces* 12 (2020) 48476–48485.
- [69] J. Zhu, J. Li, B. Chu, S. Liu, S. Fu, Q. Qin, L. Dong, B. Li, Excitation of catalytic performance on MOFs derivative carrier by residual carbon for low-temperature $\text{NH}_3\text{-SCR}$ reaction, *Mol. Catal.* 535 (2023) 112859.
- [70] Y. Zhang, M. Zhang, Y. Zeng, H. Wang, C. Liu, L. Wei, Y. Wang, L. He, W. Wang, Z. Zhang, Elimination of NH_3 by interfacial charge transfer over the Ag/CeSnO_x tandem catalyst, *ACS Catal.* 13 (2023) 1449–1461.
- [71] G. Isapour, A. Wang, J. Han, Y. Feng, H. Grönbeck, D. Creaser, L. Olsson, M. Skoglundh, H. Härelind, In situ DRIFT studies on N_2O formation over Cu-functionalized zeolites during ammonia-SCR, *Catal. Sci. Technol.* 12 (2022) 3921–3936.
- [72] S. Keller, U. Bentrup, J. Rabeha, A. Brückner, Impact of dopants on catalysts containing $\text{Ce}_{1-x}\text{M}_x\text{O}_{2.8}$ ($M = \text{Fe, Sb or Bi}$) in $\text{NH}_3\text{-SCR}$ of NO_x -A multiple spectroscopic approach, *J. Catal.* 408 (2022) 453–464.
- [73] A. Szymaszek-Wawryca, U. Díaz, D. Duraczynska, K. Świerczek, B. Samojeden, M. Motak, Catalytic performance and sulfur dioxide resistance of one-pot synthesized Fe-MCM-22 in selective catalytic reduction of nitrogen oxides with ammonia ($\text{NH}_3\text{-SCR}$)—The effect of iron content, *Int. J. Mol. Sci.* 23 (2022) 10754.
- [74] J. Schnee, L. Delannoy, G. Costentin, C. Thomas, Unraveling the direct decomposition of NO_x over keggin heteropolyacids and their deactivation using a combination of Gas-IR/MS and In situ DRIFT spectroscopy, *J. Phys. Chem. C* 124 (2020) 22459–22470.
- [75] Z. Zhi, L. Ru, W. Meng, L. Yu, J. Liu, Two steps synthesis of CeTiO_x oxides nanotube catalyst: enhanced activity, *Appl. Catal. B* 282 (2021) 119542.
- [76] Y. Yu, W. Tan, D. An, X. Wang, A. Liu, W. Zou, C. Tang, C. Ge, Q. Tong, J. Sun, Insight into the SO_2 resistance mechanism on $\gamma\text{-Fe}_2\text{O}_3$ catalyst in $\text{NH}_3\text{-SCR}$ reaction: A collaborated experimental and DFT study, *Appl. Catal. B* 281 (2021) 119544.